Kagome network of miniband-edge states in double-aligned graphene–hexagonal boron nitride structures

Christian Moulsdale [1,2,*] Angelika Knothe [2] and Vladimir Fal'ko [1,2,3]

[1]*School of Physics and Astronomy, University of Manchester, Manchester M13 9PL, United Kingdom*
[2]*National Graphene Institute, University of Manchester, Manchester M13 9PL, United Kingdom*
[3]*Henry Royce Institute, Institute for Advanced Materials, Manchester M13 9PL, United Kingdom*

Twistronic heterostructures have recently emerged as a new class of quantum electronic materials with properties determined by the twist angle between the adjacent two-dimensional materials. Here, we study moiré superlattice minibands in graphene (G) encapsulated in hexagonal boron nitride (hBN) with an almost perfect alignment with both the top and bottom hBN crystals. We show that, for such an orientation of the unit cells of the hBN layers that locally breaks inversion symmetry of the graphene lattice, the hBN/G/hBN structure features a kagome network of topologically protected states with energies near the miniband edge, propagating along the lines separating the areas with different miniband Chern numbers.

Recently, graphene-based systems have been shown to host various topological effects [1] among their electronic properties [2–21], which stem from the Berry phase/curvature in the electronic band structure of mononolayer graphene [22,23] or its Bernal bilayers [3,11,16,18,21,24–28]. The topological effects manifest themselves in states forming at the edges of the system or around internal structural defects, and propagating in opposite directions in the two valleys of graphene. These states have been studied in detail in gapped bilayer graphene with either AB/BA domain boundaries [7,8,29], or an electrostatically inverted interlayer asymmetry gap [9,30].

Topological zero line states have also emerged in the context of twistronic graphene systems [6,13,15,31–34] and in heterostructures of graphene (G) and hexagonal boron (hBN). As a result of the G-hBN lattice mismatch, $\delta \approx 0.018$, the latter system features a moiré superlattice [35–38] (mSL), even at zero misalignment angle θ. The electronic properties of this system are qualitatively modified by the mSL with a period $\lambda \approx a/\sqrt{\delta^2 + \theta^2}$, reaching 14 nm for small misalignment angles $\theta \to 0$. The system features a well-defined first miniband edge on the valence side of the graphene layer's dispersion [36,37], as illustrated in Fig. 1.

The encapsulation of graphene between two hBN crystals with a high-precision alignment [39] leads to a further refinement of the superlattice effects, caused by the interference of Dirac electrons Bragg-scattered off the moiré superlattice (mSL) determined by the top and bottom G/hBN interfaces. Here, we study the influence of the relative lateral offset τ between the top and bottom hBN crystals on moiré minibands in double-aligned hBN/G/hBN structures, considering the orientation (parallel versus antiparallel) of the unit cells in the hBN lattices. For graphene's minibands, the unit cell orientation matters due to the lack of inversion symmetry in the

hBN monolayer, which is maximally passed onto graphene encapsulated between two hBN layers with parallel unit cell orientations but mutually cancels in the antiparallel case.

The inversion asymmetry, induced by hBN in graphene, leads to minigaps at the moiré miniband edges [36] (in particular, at the bottom edge of the first miniband on the valence band side v corresponding to graphene doping of four holes per moiré supercell), of graphene's dispersion in Fig. 1, whose size, together with the Chern numbers of the minibands [40,41], depends on the lateral offset between the top and bottom hBN crystals. For hBN/G/hBN structures
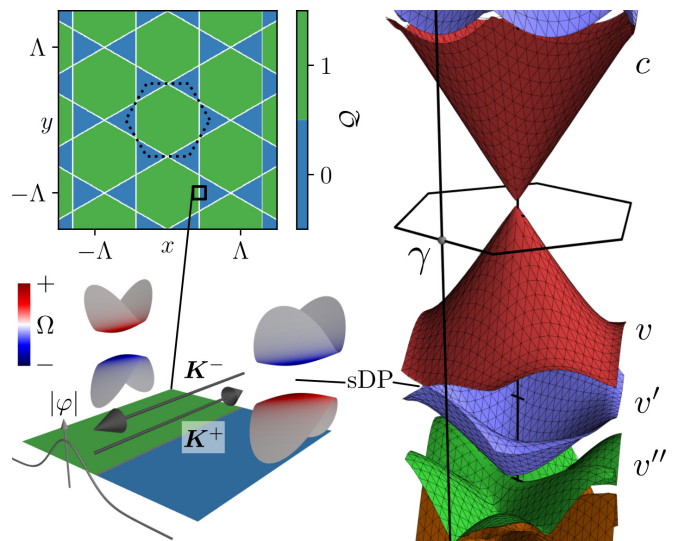

FIG. 1. A typical miniband spectrum of graphene encapsulated into mutually aligned hBN crytals. Top inset: Map of locally defined v-miniband Chern number $\mathcal{Q}$. Bottom inset: Dispersion and Berry curvature at the v/v' miniband edge in the gapped regions and 1D modes counterpropagating in $K^{\pm}$ valleys along a kagome network of locally gapless v/v' miniband edges.

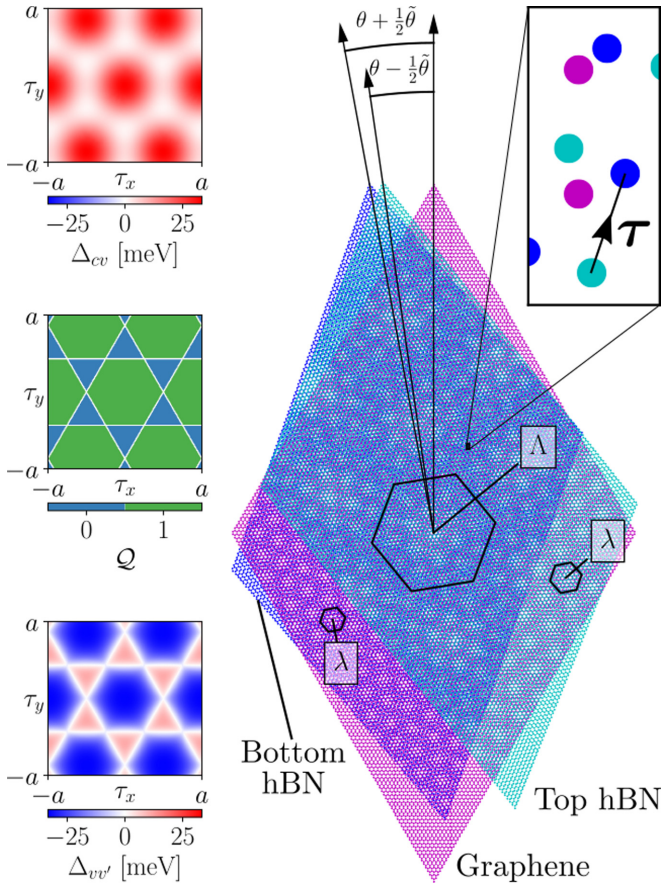*christian.moulsdale@postgrad.manchester.ac.uk

FIG. 2. Right: Graphene encapsulated between bottom and top hBN layers with twists $\theta \pm \frac{1}{2}\tilde{\theta}$, respectively ($|\tilde{\theta}| \ll \delta$). The interference of the layers results in a mSL of period λ, featuring a long-period variation of period Λ, whose unit cells are shown. Top inset: The offset vector $\boldsymbol{\tau}$ between the unit cells of the top and bottom hBN layers has components (τ_x, τ_y) along the zigzag and armchair axes, respectively. Bottom inset: The valley Chern number $\mathcal{Q}$ of miniband v, the gap Δ_{cv}, and the minigap $\Delta_{vv'}$ against offset for aligned hBN layers ($\tilde{\theta} = 0$).

with a small misalignment angle, $\tilde{\theta} \ll \delta$, between the top and bottom hBN layers, this offset varies across the coordinate space as

$$\boldsymbol{\tau}(\boldsymbol{r}) = \tilde{\theta}\boldsymbol{e}_z \times \boldsymbol{r}, \tag{1}$$

which leads to a long-period, $\Lambda \approx a/|\tilde{\theta}|$, variation of the mSL properties (see Fig. 2). A peculiar feature of this modulation is the closing and reopening of a minigap at the v/v' miniband edge, which occurs along the lines forming a kagome structure in the real space, sketched in Fig. 1. Below, we study electron states at the v/v' miniband edge, confined to this kagome network and discuss how one-dimensional (1D) states (propagating in opposite directions in the $K^{\pm}$ valleys) provide this system with a finite conductivity even when its Fermi level would be set between the v and v' miniband edges in the gapped areas of the structure, with a characteristic pattern of Aharanov-Bohm oscillations.

The above statement is based on the analysis of local miniband characteristics of the trilayer structure depicted in Fig. 2. Here, the bottom/top hBN monolayers with parallel

orientation of their nonsymmetric unit cells are twisted with respect to graphene by $\theta \pm \frac{1}{2}\tilde{\theta}$, respectively, with a small mutual misalignment $|\tilde{\theta}| \ll \delta$, which determines the spatial variation of their local offset in Eq. (1). For each fixed offset $\boldsymbol{\tau}$, the Hamiltonian [36,42–44] of electrons in the $\boldsymbol{K}^{\xi}$ valley ($\xi = \pm$) of graphene is

$$\hat{H} = -i\hbar v \boldsymbol{\sigma} \cdot \boldsymbol{\nabla} + 2 \sum_{\mathcal{P}=\pm} \sum_{m=0}^{5} \mathfrak{C}_m e^{i\boldsymbol{G}_m \cdot \boldsymbol{r}} U_{\mathcal{P},m} + \frac{1}{2}\Delta_{cv}\sigma_z,$$

$$U_{\mathcal{P},m} = u_0^{\mathcal{P}} \mathcal{P}^{m+\frac{1}{2}} + (-\mathcal{P})^{m+\frac{1}{2}} \left(u_3^{\mathcal{P}}\sigma_z - i\xi u_1^{\mathcal{P}}\boldsymbol{e}_m \cdot \boldsymbol{\sigma} \right),$$

$$\boldsymbol{\sigma} = (\xi\sigma_x, \sigma_y), \quad \Delta_{cv} \approx \frac{2}{3}\sum_{m=0}^{5}\left(\mathfrak{C}_m^2 \Delta_u - \mathfrak{S}_m^2 \Delta_h \right),$$

$$\mathfrak{C}_m = \cos\left(\frac{1}{2}\boldsymbol{g}_m \cdot \boldsymbol{\tau}\right), \quad \mathfrak{S}_m = \sin\left(\frac{1}{2}\boldsymbol{g}_m \cdot \boldsymbol{\tau}\right). \tag{2}$$

The values of the parameters used are given in Table S1 in the Supplemental Material (SM) [45] (see also Refs. [4,36,37,40,41,44,46–52] therein), and the expression for graphene encapsulated between hBN monolayers with antiparallel orientation of their unit cells is given in SM S2 [45].

The first term in Eq. (2) is the Dirac Hamiltonian for electrons in monolayer graphene [42]. The second term describes the mSL produced by the layers, with the reciprocal mSL vectors, $\boldsymbol{G}_m \approx \delta\boldsymbol{g}_m - \theta\boldsymbol{e}_z \times \boldsymbol{g}_m$, expressed in terms of the reciprocal lattice vectors of graphene, $\boldsymbol{g}_m = \frac{4\pi}{\sqrt{3}a}\boldsymbol{e}_z \times \boldsymbol{e}_m$, $\boldsymbol{e}_m = (\cos\frac{m\pi}{3}, \sin\frac{m\pi}{3})$, $m = 0, 1, \ldots, 5$. This term includes mSL potentials, sublattice asymmetry gaps, and gauge fields of parity $\mathcal{P} = \pm$ (under spatial inversion), quantified using the parameters $u_0^{\mathcal{P}}$, $u_3^{\mathcal{P}}$, and $u_1^{\mathcal{P}}$, respectively.

The orientation and offset $\boldsymbol{\tau}$ of the unit cells in each hBN layer determine the magnitude of the odd-parity terms in Eq. (2), which are responsible for the inversion symmetry breaking features in the dispersion, such as the opening of a minigap between minibands v and v'. This corresponds to graphene doping of four holes per moiré supercell, with electron density $-4n_0$ ($n_0 = 2/\sqrt{3}\lambda^2$). In the parametrization of Hamiltonian (2), we take into account that the positions of the graphene atoms rearrange to minimize graphene's adhesion energy with the hBN layers while maintaining the mSL period [44,53–55]. The in-plane and out-of-plane rearrangements combine with the second term to give the respective contributions Δ_u and Δ_h to the sublattice asymmetry gap Δ_{cv}. This gap appears in the odd-parity, nonoscillatory third term, which breaks the sublattice symmetry of graphene. In antiparallel alignment, the contributions to the odd-parity terms from each layer cancel, and inversion symmetry is preserved. Instead, we focus on parallel alignment where the inversion symmetry breaking is enhanced, depending strongly on the offset $\boldsymbol{\tau}$.

To study the minibands of Dirac electrons in this system, we diagonalize Hamiltonian (2) using the basis of plane-wave Dirac states, folded onto the mSL Brillouin zone shown in Fig. 1. An example of a typical miniband dispersion is shown in Fig. 1, with other examples displayed in SM S3 [45]. Similarly to single-interface G/hBN heterostructures [35–37,56–59], this system features a well-defined first

valence miniband v for twists $|\theta| \lesssim 1°$, whereas on the conduction band side the minibands strongly overlap on the energy axis. The inversion symmetry breaking produces a minigap $\Delta_{vv'}$ at the edge between minibands v and v', whose magnitude, together with the v/v' edge position in the Brillouin minizone, depends on the offset $\boldsymbol{\tau}$. The dependence of the minigap $\Delta_{vv'}$ on the offset $\boldsymbol{\tau}$ is shown in the bottom inset of Fig. 2. This panel shows that $\Delta_{vv'}$ (which is formally defined below) takes zero value and also changes sign on the lines which approximately correspond to the condition $\mathfrak{C}_m = 0$. This variation should be contrasted with the $\boldsymbol{\tau}$ dependence of the gap Δ_{cv} across the main Dirac point at the c/v miniband edge shown on the top inset, where one can see that Δ_{cv} never changes sign.

Along the lines on the $\boldsymbol{\tau}$ maps, where the minigap at the v/v' miniband edge closes and reopens as a function of $\boldsymbol{\tau}$, the Chern number $\xi\mathcal{Q}$ [40,41] of miniband v also changes (note that the miniband's Chern number has opposite sign in the K^{ξ} valleys, $\xi = \pm$). Here, $\mathcal{Q}$ is found by computing the integral of the miniband's Berry curvature over the mSL Brillouin minizone (see SM S4 [45] for details). The resulting map of $\mathcal{Q}(\boldsymbol{\tau})$ dependence is displayed as the middle inset in Fig. 2. The correlation between the behavior of the inversion-asymmetry gap $\Delta_{vv'}$ at its edge with miniband v' and of its Chern number suggests a simultaneous change of quantum topological properties of states in both v and v', captured by the effective Hamiltonian [50] applicable to the part of the Brillouin minizone in the vicinity of this edge,

$$H_{\boldsymbol{q}}^{vv'} = \epsilon_{vv'} + \tfrac{1}{2}\Delta_{vv'}\sigma_z + \hbar\big(\xi v_s^x q_x \sigma_x + v_s^y q_y \sigma_y\big) + \xi\hbar\boldsymbol{v}_a \cdot \boldsymbol{q}, \tag{3}$$

whose basis is minibands v and v'. Here, $\boldsymbol{q}$ is the wave vector relative to the position of the band edge, $\boldsymbol{v}_s$ and $\boldsymbol{v}_a$ are the symmetric and antisymmetric velocities, respectively (the latter of which tilts the dispersion along the axis parallel to $\boldsymbol{v}_a$ [50]), and $\epsilon_{vv'}$ is a constant energy shift. The parameters in Eq. (3) are fitted numerically to the minibands computed using Eq. (2) (see SM S5 [45]). The sign of $\Delta_{vv'}$ is determined by the sign of the Berry curvature at the miniband edge, which changes simultaneously with the change of the Chern number.

The variation of the offset $\boldsymbol{\tau}$ over the plane of a hBN/G/hBN structure, given by Eq. (1), enables us to map the the computed dependence of miniband characteristics displayed on the insets in Fig. 2 onto the real space: For this, we only need to rotate those plots by $90°$ and rescale them by a factor $1/\tilde{\theta}$. This produces a kagome network of lines where the secondary minigap $\Delta_{vv'}$ closes and then inverts its sign, and where the Chern number of miniband v changes (from 0 to 1). We show in SM S6 [45] that the shape of this network is independent of the model parameters. Topologically protected channels form along these lines, supporting spin-degenerate, one-dimensional states which propagate in opposite directions in the time-reversed valleys.

The form and dispersion of these states can be found (in SM S7 [45]) by analyzing Hamiltonian (3) with $\boldsymbol{q} \approx (q_{\|}, -i\partial_{x_{\perp}})$ and $\Delta_{vv'} \approx x_{\perp}\partial_{x_{\perp}}\Delta_{vv'}|_{x_{\perp}=0}$ ($\partial_{x_{\perp}}\Delta_{vv'}|_{x_{\perp}=0} \sim |u_3^-|/\Lambda > 0$) where $x_{\|}$ and $x_{\perp}$ are local coordinates along and perpendicular to the kagome network line. These states have a Jackiw-Rebbi [46] form $\varphi_{q_{\|}} \approx e^{iq_{\|}x_{\|}}e^{-x_{\perp}^2/2\aleph^2}\zeta_{q_{\|}}$ ($\zeta_{q_{\|}}$ is a two-component vector), with Gaussian confinement within a
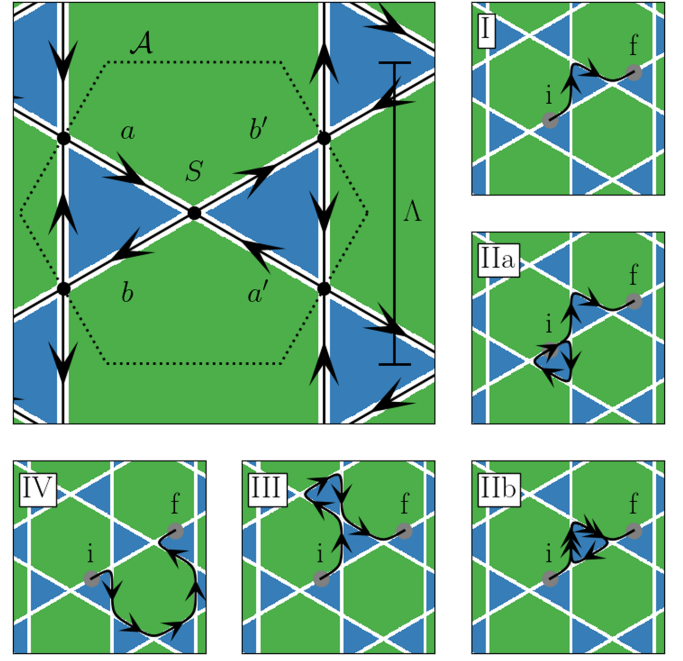

FIG. 3. Top left: The hexagonal structural element of the kagome network of channels of area $\mathcal{A} = \sqrt{3}\Lambda^2/2$ and containing one $\mathcal{Q} = 0$ bowtie and one $\mathcal{Q} = 1$ hexagon. The propagation of electrons in the $\boldsymbol{K}_+$ valley is shown, scattering at the three nodes. Clockwise from top right: The five shortest paths for an electron wave packet to propagate from an injection position "i" to "f" (double arrows indicate a channel is traversed twice).

length $\aleph \sim \sqrt{2\hbar v_s^x \Lambda/|u_3^-|}$ perpendicular to the interface, and disperse linearly, $\epsilon(q_{\|}) = \xi\hbar\mathcal{V}q_{\|}$, with a 1D velocity $\mathcal{V} \sim v_s^x$. To consider these states independently for each segment of the kagome network, we should require $\lambda < \aleph \ll \Lambda$, which is satisfied for mismatches $|\tilde{\theta}| < 0.1°$.

For a gapped moiré miniband spectrum, one could expect insulating behavior of a perfectly aligned hBN/G/hBN doped to the v/v' miniband edge. For slightly ($|\tilde{\theta}| \ll \delta$) misaligned hBN crystals, the long-range variation of the local hBN-hBN offset and a network of states, which it generates inside the minigap $\Delta_{vv'}$, quenches the resistivity of the hBN/G/hBN structure. While the exact calculations of the limiting resistivity would require a more rigorous consideration, based on the previous experiences of two-dimensional models for the network of 1D states [31,32,60], we expect its value to correspond to a conductivity $\sigma_{xx} \sim e^2/h$ and to exhibit Aharonov-Bohm oscillations as a function of an out-of-plane magnetic field B. To describe the latter, we consider coherent electron waves (separately in the $\boldsymbol{K}_{\pm}$ valleys) on a network sketched in Fig. 3, where the structural element includes three nodes connected by channels. At each node, an incoming wave packet scatters left or right according to the scattering matrix

$$\binom{b}{b'} = S\binom{a}{a'}, \quad S = e^{i\eta/3}\begin{pmatrix} \sqrt{P_R} & i\sqrt{P_L} \\ i\sqrt{P_L} & \sqrt{P_R} \end{pmatrix}, \tag{4}$$

whose factor of i takes into account the Maslov's phase, and whose scattering probabilities, P_R and P_L ($P_R + P_L = 1$), can

be considered as energy-independent within the narrow energy window of $\Delta_{vv'}$ (see SM S8 [45] for details).

As a monochromatic wave of energy ϵ propagates across the network, its amplitude evolves according to the scattering matrix at the nodes and acquiring phase factors, $e^{i\epsilon\Lambda/2\mathcal{V}}$, after passing each ballistic segment of the network. At longer distances, partial waves, e.g., split from an incoming wave at "i" (see the side panels in Fig. 3), rejoin and interfere in another ballistic segment "f." An important feature of a periodic and C_3 rotationally symmetric network, such as in Figs. 1 and 3, is that the effect of the interference, constructive or destructive, of edge states that travel from i to f along paths containing the same number N of segments does not depend on the exact energy (or wavelength) of the electron. This is because their ballistic phases $e^{iN\epsilon\Lambda/2\mathcal{V}}$ are the same, producing the interference contribution determined only by their shapes through the energy-independent scattering amplitudes in Eq. (4). On the contrary, the interference of waves brought together by paths with a different number of segments (such as I and IV in Fig. 3) oscillates from constructive to destructive (and back) upon energy variation at the scale of $\hbar\mathcal{V}/\Lambda$.

Therefore, in the high-temperature regime, where $k_B T \gg \hbar\mathcal{V}/\Lambda$, the interference effects between waves arriving from i to f along paths of different lengths would be wiped out by the smearing of the Fermi step for electrons. The interference between waves brought from i to f by same-length paths (such as IIa, IIb, III, and IV in Fig. 3) would survive thermal averaging, without suppression, though this contribution would be sensitive to the external magnetic field, due to the Aharonov-Bohm phases from magnetic field fluxes encircled by the pairs of same-length paths.

When discussing the interference effects in electronic transport at high temperatures, we are also conscious of the inelastic decoherence of electron waves, which efficiently destroys interference effects for the longer paths. For a system with decoherence length ℓ, this can be accounted by a suppression factor $e^{-\Lambda/4\ell}$ applied to each ballistic segment of the kagome network. Therefore, to discuss the high-temperature limit, we consider the shortest paths that can contribute to the interference effect in transport, shown in the side panels of Fig. 3. These paths are related to the "forward" electron propagation from a segment in one network unit cell to the equivalent segment in the next one, counted in the direction of the propagation of the edge state (for valley K). These shortest paths contain three (I) and six (IIa, IIb, III, IV) ballistic segments of length $\Lambda/2$, and the interfering amplitude at the point f for a wave starting at i with unit amplitude would be

$$\psi \approx -e^{i\pi\phi/4\phi_0}\sqrt{P_L^2 P_R}z^3 + z^6 e^{i\pi\phi/2\phi_0}$$
$$\times \left(-2P_L P_R^2 + P_L^2 P_R + e^{-i2\pi\phi/\phi_0}P_L^2 P_R\right),$$

where $z = e^{i\eta/3}e^{i\epsilon\Lambda/2\hbar\mathcal{V}}e^{-\Lambda/4\ell}$. We also account for additional phases, induced by the out-of-plane magnetic field and de-

scribed in terms of magnetic field flux $\phi = B\mathcal{A}$ through the unit cell area $\mathcal{A} = \sqrt{3}\Lambda^2/2$ of the kagome network ($\phi_0 = h/e$ is the flux quantum).

Then, we express the probability $\langle\mathcal{W}\rangle_T$ for the electron to get from the segment i to f, averaged over the $k_B T$ energy interval near the Fermi level, as

$$\langle\mathcal{W}\rangle_T \approx P_L^2 P_R|z|^6 + \left[4P_L^2 P_R^4 + 2P_L^4 P_R^2\right]|z|^{12}$$
$$+ 2\left[P_L^4 P_R^2 - 2P_L^3 P_R^3\right]|z|^{12}\cos\left(\frac{2\pi\phi}{\phi_0}\right), \quad (5)$$

whose second line originates from the encircled Aharonov-Bohm phases, which, for the pairs of shortest paths, are all determined by the magnetic field flux through the unit cell area of the kagome network. As the probability, described by Eq. (5), is a characteristic of the forward propagation of electrons, its oscillations also determine the Aharonov-Bohm oscillations in the network conductivity (see SM S9 [45] for backwards propagation),

$$\sigma_{xx}(\phi) \approx \frac{e^2}{h}\left[\alpha + \beta e^{-5\Lambda/2\ell}\cos\left(\frac{2\pi\phi}{\phi_0}\right)\right], \quad (6)$$

where $\alpha, \beta \sim 1$.

Overall, we have demonstrated the existence of a kagome network of states lying in the minigap at the edge of the first moiré miniband on the valence band side of graphene encapsulated between hBN with parallel unit cells. This edge state network gives rise to quenched resistivity, $\sim h/e^2$, of graphene even when its Fermi level doping reaches that minigap. This conductivity, in Eq. (6), exhibits Aharonov-Bohm oscillations, whose period is determined by the area of the unit cell of the kagome network and, consequently, the misalignment. For the networks with a longer decay length ℓ (or a shorter period), the magnitude of the Aharonov-Bohm oscillations should increase, accompanied by the emergence of a finer structure, composed of higher-frequency harmonics corresponding to the rational factor between the magnetic field flux through the kagome network cell and flux quantum ϕ_0. Such edge state networks emphasize the role of twistronic heterostructures as hosts of topological phenomena and deserve further theoretical studies, e.g., taking into account electron-electron interactions in the channels [61–65], as well as the effects of edge states at the physical edge of a finite system [66].

[1] L. Fu and C. L. Kane, Phys. Rev. B **76**, 045302 (2007).

[2] Y. Zhang, Y.-W. Tan, H. L. Stormer, and P. Kim, Nature (London) **438**, 201 (2005).

[3] K. S. Novoselov, E. McCann, S. V. Morozov, V. I. Fal'ko, M. I. Katsnelson, U. Zeitler, D. Jiang, F. Schedin, and A. K. Geim, Nat. Phys. **2**, 177 (2006).

[4] D. Xiao, W. Yao, and Q. Niu, Phys. Rev. Lett. **99**, 236809 (2007).

[5] J. Li, I. Martin, M. Büttiker, and A. F. Morpurgo, Nat. Phys. **7**, 38 (2011).

[6] P. San-Jose and E. Prada, Phys. Rev. B **88**, 121408(R) (2013).

[7] L. Ju, Z. Shi, N. Nair, Y. Lv, C. Jin, J. Velasco, C. Ojeda-Aristizabal, H. A. Bechtel, M. C. Martin, A. Zettl, J. Analytis, and F. Wang, Nature (London) **520**, 650 (2015).

[8] L.-J. Yin, H. Jiang, J.-B. Qiao, and L. He, Nat. Commun. **7**, 11760 (2016).

[9] J. Li, K. Wang, K. J. McFaul, Z. Zern, Y. Ren, K. Watanabe, T. Taniguchi, Z. Qiao, and J. Zhu, Nat. Nanotechnol. **11**, 1060 (2016).

[10] M. Eich, F. Herman, R. Pisoni, H. Overweg, A. Kurzmann, Y. Lee, P. Rickhaus, K. Watanabe, T. Taniguchi, M. Sigrist, T. Ihn, and K. Ensslin, Phys. Rev. X **8**, 031023 (2018).

[11] A. Knothe and V. Fal'ko, Phys. Rev. B **98**, 155435 (2018).

[12] R. Kraft, I. V. Krainov, V. Gall, A. P. Dmitriev, R. Krupke, I. V. Gornyi, and R. Danneau, Phys. Rev. Lett. **121**, 257703 (2018).

[13] S. Huang, K. Kim, D. K. Efimkin, T. Lovorn, T. Taniguchi, K. Watanabe, A. H. MacDonald, E. Tutuc, and B. J. LeRoy, Phys. Rev. Lett. **121**, 037702 (2018).

[14] K. Komatsu, Y. Morita, E. Watanabe, D. Tsuya, K. Watanabe, T. Taniguchi, and S. Moriyama, Sci. Adv. **4**, eaaq0194 (2018).

[15] D. K. Efimkin and A. H. MacDonald, Phys. Rev. B **98**, 035404 (2018).

[16] H. Overweg, A. Knothe, T. Fabian, L. Linhart, P. Rickhaus, L. Wernli, K. Watanabe, T. Taniguchi, D. Sánchez, J. Burgdörfer, F. Libisch, V. I. Fal'ko, K. Ensslin, and T. Ihn, Phys. Rev. Lett. **121**, 257702 (2018).

[17] C. Dutreix, H. González-Herrero, I. Brihuega, M. I. Katsnelson, C. Chapelier, and V. T. Renard, Nature (London) **574**, 219 (2019).

[18] Y. Lee, A. Knothe, H. Overweg, M. Eich, C. Gold, A. Kurzmann, V. Klasovika, T. Taniguchi, K. Wantanabe, V. Fal'ko, T. Ihn, K. Ensslin, and P. Rickhaus, Phys. Rev. Lett. **124**, 126802 (2020).

[19] Y. Shi, S. Xu, Y. Yang, S. Slizovskiy, S. V. Morozov, S.-K. Son, S. Ozdemir, C. Mullan, J. Barrier, J. Yin, A. I. Berdyugin, B. A. Piot, T. Taniguchi, K. Watanabe, V. I. Fal'ko, K. S. Novoselov, A. K. Geim, and A. Mishchenko, Nature (London) **584**, 210 (2020).

[20] Y. Li, M. Amado, T. Hyart, G. P. Mazur, and J. W. A. Robinson, Commun. Phys. **3**, 224 (2020).

[21] C. Tong, R. Garreis, A. Knothe, M. Eich, A. Sacchi, K. Watanabe, T. Taniguchi, V. Fal'ko, T. Ihn, K. Ensslin, and A. Kurzmann, Nano Lett. **21**, 1068 (2021).

[22] D. P. DiVincenzo and E. J. Mele, Phys. Rev. B **29**, 1685 (1984).

[23] T. Ando, T. Nakanishi, and R. Saito, J. Phys. Soc. Jpn. **67**, 2857 (1998).

[24] E. McCann and V. I. Fal'ko, Phys. Rev. Lett. **96**, 086805 (2006).

[25] M. Mucha-Kruczyński, I. L. Aleiner, and V. I. Fal'ko, Phys. Rev. B **84**, 041404(R) (2011).

[26] C. Moulsdale, A. Knothe, and V. Fal'ko, Phys. Rev. B **101**, 085118 (2020).

[27] A. Knothe and V. Fal'ko, Phys. Rev. B **101**, 235423 (2020).

[28] A. Knothe, L. I. Glazman, and V. I. Fal'ko, arXiv:2104.03399.

[29] F. Zhang, A. H. MacDonald, and E. J. Mele, Proc. Natl. Acad. Sci. USA **110**, 10546 (2013).

[30] I. Martin, Y. M. Blanter, and A. F. Morpurgo, Phys. Rev. Lett. **100**, 036804 (2008).

[31] C. De Beule, F. Dominguez, and P. Recher, Phys. Rev. Lett. **125**, 096402 (2020).

[32] C. De Beule, F. Dominguez, and P. Recher, Phys. Rev. B **104**, 195410 (2021).

[33] N. R. Walet and F. Guinea, 2D Mater. **7**, 015023 (2019).

[34] S. G. Xu, A. I. Berdyugin, P. Kumaravadivel, F. Guinea, R. Krishna Kumar, D. A. Bandurin, S. V. Morozov, W. Kuang, B. Tsim, S. Liu, J. H. Edgar, I. V. Grigorieva, V. I. Fal'ko, M. Kim, and A. K. Geim, Nat. Commun. **10**, 4008 (2019).

[35] M. Yankowitz, J. Xue, D. Cormode, J. D. Sanchez-Yamagishi, K. Watanabe, T. Taniguchi, P. Jarillo-Herrero, P. Jacquod, and B. J. LeRoy, Nat. Phys. **8**, 382 (2012).

[36] J. R. Wallbank, A. A. Patel, M. Mucha-Kruczyński, A. K. Geim, and V. I. Fal'ko, Phys. Rev. B **87**, 245408 (2013).

[37] M. Lee, J. R. Wallbank, P. Gallagher, K. Watanabe, T. Taniguchi, V. I. Fal'ko, and D. Goldhaber-Gordon, Science **353**, 1526 (2016).

[38] Y.-N. Ren, Y. Zhang, Y.-W. Liu, and L. He, Chin. Phys. B **29**, 117303 (2020).

[39] Y. Yang, J. Li, J. Yin, S. Xu, C. Mullan, T. Taniguchi, K. Watanabe, A. K. Geim, K. S. Novoselov, and A. Mishchenko, Sci. Adv. **6**, eabd3655 (2020).

[40] T. Fukui, Y. Hatsugai, and H. Suzuki, J. Phys. Soc. Jpn. **74**, 1674 (2005).

[41] Y. Ren, Z. Qiao, and Q. Niu, Rep. Prog. Phys. **79**, 066501 (2016).

[42] J. W. McClure, Phys. Rev. **104**, 666 (1956).

[43] J. Wallbank, M. Mucha-Kruczynski, X. Chen, and V. Fal'ko, Ann. Phys. **527**, 359 (2015).

[44] M. Szyniszewski, E. Mostaani, A. Knothe, V. Enaldiev, A. C. Ferrari, V. I. Fal'ko, and N. D. Drummond (unpublished).

[45] See Supplemental Material at http://link.aps.org/supplemental/10.1103/PhysRevB.105.L201112 for additional details on the theoretical techniques used in this Letter, alongside more examples of the band structure for parallel and antiparallel orientation of the hBN unit cells.

[46] R. Jackiw and C. Rebbi, Phys. Rev. D **13**, 3398 (1976).

[47] D. J. Thouless, M. Kohmoto, M. P. Nightingale, and M. den Nijs, Phys. Rev. Lett. **49**, 405 (1982).

[48] M. V. Berry, Proc. R. Soc. London, Ser. A **392**, 45 (1984).

[49] M. Kohmoto, Ann. Phys. **160**, 343 (1985).

[50] M. O. Goerbig, J.-N. Fuchs, G. Montambaux, and F. Piéchon, Phys. Rev. B **78**, 045415 (2008).

[51] A. H. Castro Neto, F. Guinea, N. M. R. Peres, K. S. Novoselov, and A. K. Geim, Rev. Mod. Phys. **81**, 109 (2009).

[52] D. Xiao, M.-C. Chang, and Q. Niu, Rev. Mod. Phys. **82**, 1959 (2010).

[53] P. San-Jose, A. Gutiérrez-Rubio, M. Sturla, and F. Guinea, Phys. Rev. B **90**, 075428 (2014).

[54] P. San-Jose, A. Gutiérrez-Rubio, M. Sturla, and F. Guinea, Phys. Rev. B **90**, 115152 (2014).

[55] J. Jung, A. M. DaSilva, A. H. MacDonald, and S. Adam, Nat. Commun. **6**, 6308 (2015).

[56] L. A. Ponomarenko, R. V. Gorbachev, G. L. Yu, D. C. Elias, R. Jalil, A. A. Patel, A. Mishchenko, A. S. Mayorov, C. R. Woods, J. R. Wallbank, M. Mucha-Kruczynski, B. A. Piot, M. Potemski, I. V. Grigorieva, K. S. Novoselov, F. Guinea, V. I. Fal'ko, and A. K. Geim, Nature (London) **497**, 594 (2013).

[57] M. S. Fuhrer, Science **340**, 1413 (2013).

[58] W. Yang, G. Chen, Z. Shi, C.-C. Liu, L. Zhang, G. Xie, M. Cheng, D. Wang, R. Yang, D. Shi, K. Watanabe, T. Taniguchi, Y. Yao, Y. Zhang, and G. Zhang, Nat. Mater. **12**, 792 (2013).

[59] G. L. Yu, R. V. Gorbachev, J. S. Tu, A. V. Kretinin, Y. Cao, R. Jalil, F. Withers, L. A. Ponomarenko, B. A. Piot, M. Potemski, D. C. Elias, X. Chen, K. Watanabe, T. Taniguchi, I. V. Grigorieva, K. S. Novoselov, V. I. Fal'ko, A. K. Geim, and A. Mishchenko, Nat. Phys. **10**, 525 (2014).

[60] J. M. Lee, M. Oshikawa, and G. Y. Cho, Phys. Rev. Lett. **126**, 186601 (2021).

[61] M. Killi, T.-C. Wei, I. Affleck, and A. Paramekanti, Phys. Rev. Lett. **104**, 216406 (2010).

[62] X.-C. Wu, C.-M. Jian, and C. Xu, Phys. Rev. B **99**, 161405(R) (2019).

[63] Y.-Z. Chou, Y.-P. Lin, S. Das Sarma, and R. M. Nandkishore, Phys. Rev. B **100**, 115128 (2019).

[64] E. J. König, P. Coleman, and A. M. Tsvelik, Phys. Rev. B **102**, 104514 (2020).

[65] Y.-Z. Chou, F. Wu, and J. D. Sau, Phys. Rev. B **104**, 045146 (2021).

[66] T. Hou, Y. Ren, Y. Quan, J. Jung, W. Ren, and Z. Qiao, Phys. Rev. B **101**, 201403(R) (2020).